The Astrophysical Journal, 923:227 (9pp), 2021 December 20 https://doi.org/10.3847/1538-4357/ac3142

Annihilation of Magnetic Islands at the Top of Solar Flare Loops

Yulei Wang[1,2], Xin Cheng[1,2], Mingde Ding[1,2], and Quanming Lu[3,4]
[1] School of Astronomy and Space Science, Nanjing University, Nanjing 210023, People's Republic of China; xincheng@nju.edu.cn
[2] Key Laboratory for Modern Astronomy and Astrophysics (Nanjing University), Ministry of Education, Nanjing 210023, People's Republic of China
[3] CAS Key Laboratory of Geospace Environment, Department of Geophysics and Planetary Science, University of Science and Technology of China, Hefei 230026, People's Republic of China
[4] CAS Center for Excellence in Comparative Planetology, People's Republic of China
Received 2021 August 12; revised 2021 October 16; accepted 2021 October 18; published 2021 December 24

Abstract

The dynamics of magnetic reconnection in the solar current sheet (CS) is studied by high-resolution 2.5-dimensional MHD simulation. With the commencing of magnetic reconnection, a number of magnetic islands are formed intermittently and move quickly upward and downward along the CS. Upon collision with the semi-closed flux of the flare loops, the downflow islands cause a second reconnection with a rate comparable with that in the main CS. Though the time-integrated magnetic energy release is still dominated by the reconnection in the main CS, the second reconnection can release substantial magnetic energy, annihilating the main islands and generating secondary islands with various scales at the flare loop top. The distribution function of the flux of the secondary islands is found to follow a power law varying from $f(\psi) \sim \psi^{-1}$ (small scale) to ψ^{-2} (large scale), which seems to be independent to background plasma β and thermal conduction (TC). However, the spatial scale and the strength of the termination shocks driven by the main reconnection outflows or islands decrease if β increases or if TC is included. We suggest that the annihilation of magnetic islands at the flare loop top, which is not included in the standard flare model, plays a nonnegligible role in releasing magnetic energy to heat flare plasma and accelerate particles.

Unified Astronomy Thesaurus concepts: Solar flares (1496); Solar magnetic reconnection (1504); Magnetohydrodynamical simulations (1966)

Supporting material: animation

1. Introduction

Magnetic reconnection, a fundamental energy-releasing process in magnetized plasma, is believed to be the core mechanism driving solar eruptions, including solar flares, coronal mass ejections (CMEs), and other solar activities. According to the standard flare model, the sheared magnetic field is stretched and forms a large-scale thin current sheet (CS) in the wake of the eruption (Kopp & Pneuman 1976; Lin & Forbes 2000; Lin et al. 2015). The reconnection in the CS in turn drives a CME eruption and the formation of flare loops. Theoretically, a squeezed thin CS becomes unstable as the tearing mode instability grows (Priest & Forbes 2000; Pucci & Velli 2013; Loureiro & Uzdensky 2015). In particular, in a high-Lundquist-number corona, the plasmoid instability will dominate the dynamics of the magnetic reconnection (Bhattacharjee et al. 2009; Samtaney et al. 2009; Huang & Bhattacharjee 2010; Huang et al. 2011; Shen et al. 2011; Huang & Bhattacharjee 2013, 2012; Loureiro & Uzdensky 2015; Huang et al. 2017; Zhao & Keppens 2020). The classical CS predicted by Sweet–Parker is thus split and the reconnection enters into a fast scheme and generates a number of magnetic islands.

Magnetic islands are believed to be closely related to fine structures in the CS (Shen et al. 2011; Lin et al. 2015). The coalescence of magnetic islands can further produce secondary CSs and islands (Bárta et al. 2011). Various researchers have analyzed the cascading law of magnetic island flux theoretically or numerically, which predicts that the distribution function of the magnetic island flux $f(\psi)$ in the CS follows a power law between ψ^{-1} to ψ^{-2} (e.g., Uzdensky et al. 2010; Huang & Bhattacharjee 2012; Shen et al. 2013; Lynch et al. 2016; Ye et al. 2019). The fragmented and turbulent characteristics of the CS have also been suggested by recent observations (e.g., Cheng et al. 2018).

The flare loop top, interacting with the reconnection downflows, also shows complex dynamics. The turbulent characteristics of the loop top have been studied by high-resolution simulations (e.g., Cai et al. 2019; Ye et al. 2020; Cai et al. 2021). The generation of flare quasi-periodic pulsations (QPPs) and the supra-arcade downflows above the flare loop top is interpreted to be closely related to the fast reconnection downflows (Takasao & Shibata 2016; Guo et al. 2014). Abundant MHD shocks have been predicted by simulations (Takasao et al. 2015). In particular, as an important prediction of the standard solar flare model, fast mode termination shocks (TSs), formed when the downflows hit the relatively steady high-density structure at the loop top, are believed to be an effective mechanism to accelerate particles (Tsuneta & Naito 1998; Shen et al. 2018; Kong et al. 2019, 2020; Ruan et al. 2020), which are supported by radio imaging observations (Aurass & Mann 2004; Chen et al. 2015). The downflow magnetic islands also affect the dynamics of the flare loops (Cai et al. 2019; Ye et al. 2020), the formation of TSs (Shen et al. 2018), and even the acceleration of energetic electrons (Kong et al. 2020).

Nevertheless, mainly owing to the limitation of observations and simulations, magnetic reconnection in the CS and its relation to the dynamics at the flare loop top are still far from

being fully understood. In this paper, we perform high-resolution 2.5-dimensional MHD simulations of the CS reconnection in a high-Lundquist-number and low-β coronal environment and focus on the dynamics of magnetic islands evolving toward flare loops. We find that the downflow magnetic islands quickly annihilate after colliding with the tip of cusp-shaped flare loops. Such a second reconnection process is characterized by horizontal CSs, smaller-scale islands, and a comparable reconnection rate with that in the main CS. In Section 2, we describe our method. Section 3 presents the main results, which are followed by a summary and discussion.

2. Method

In this work, the MHD equation we solve is as follows:

$$\begin{aligned}
\frac{\partial \rho}{\partial t} + \nabla \cdot (\rho \boldsymbol{u}) &= 0, \\
\frac{\partial (\rho \boldsymbol{u})}{\partial t} + \nabla \cdot (\rho \boldsymbol{u}\boldsymbol{u} - \boldsymbol{B}\boldsymbol{B} + P^*) &= 0, \\
\frac{\partial e}{\partial t} + \nabla \cdot [(e + P^*)\boldsymbol{u} - \boldsymbol{B}(\boldsymbol{B} \cdot \boldsymbol{u})] &= \nabla \cdot (\kappa_{\parallel} \hat{\boldsymbol{b}}\hat{\boldsymbol{b}} \cdot \nabla T), \\
\frac{\partial \boldsymbol{B}}{\partial t} - \nabla \times (\boldsymbol{u} \times \boldsymbol{B}) &= -\nabla \times (\eta \boldsymbol{J}), \\
\boldsymbol{J} &= \nabla \times \boldsymbol{B},
\end{aligned} \tag{1}$$

where $\boldsymbol{P}^* = (p + B^2/2)\boldsymbol{I}$, $e = p/(\gamma - 1) + \rho u^2/2 + B^2/2$, $\kappa_{\parallel} = \kappa_0 T^{2.5}$, and standard notations of variables are used. In our model, only the thermal conduction (TC) along the magnetic field is considered, which is much more important than the perpendicular components, and κ_0 is set as $10^6\,\mathrm{erg \cdot s^{-1}\,cm^{-1}\,K^{-3.5}}$ (Yokoyama & Shibata 2001). Here, all variables have been normalized according to constant units. The unit of space is chosen as the scale of simulation region $L_0 = 5 \times 10^9$ cm, which is comparable with the value for a typical observed flare event (see Cheng et al. 2018). We also assume that the coronal plasma is composed of fully ionized hydrogen with an electron density $n_e = 10^{10}\,\mathrm{cm^{-3}}$ and an average particle mass $\bar{m} = 0.5 m_p = 8.36 \times 10^{-25}$ g, which gives a unit of mass density $\rho_0 = 2 n_e \bar{m} = 1.67 \times 10^{-14}\,\mathrm{g/cm^3}$ (Priest & Forbes 2000). Here, m_p is the proton mass. The unit of magnetic strength is set as a typical coronal value, namely $B_0 = 20$ Gauss (also see Chen et al. 1999; Ye et al. 2020). Based on L_0, $\bar{m}$, ρ_0, and B_0, normalized units of other variables are deduced as $u_0 = B_0/\sqrt{\mu_0 \rho_0} = 4.36 \times 10^7\,\mathrm{cm/s}$, $t_0 = L_0/u_0 = 114.61$ s, $p_0 = \rho_0 u_0^2 = 3.18$ Pa, $T_0 = \bar{m} u_0^2/k_B = 11.52$ MK, $\kappa_{\parallel 0} = k_B \rho_0 u_0 L_0/\bar{m} = 6.02 \times 10^{11}\,\mathrm{erg/s \cdot cm \cdot K}$, and $\eta_0 = L_0 u_0 = 2.18 \times 10^{17}\,\mathrm{cm^2/s}$, where μ_0 is the magnetic permeability in vacuum and k_B denotes the Boltzmann constant. The ratio of specific heat is $\gamma = 5/3$. Under this configuration, the unit time, velocity, and temperature are also on the same order as the observational ones given by Cheng et al. (2018).

The initial magnetic field is set according to the CSHKP model (Chen et al. 1999; Ye et al. 2020)

Table 1
Configurations of All Simulation Cases

Cases	p_b	β	TC
1	0.02	0.04	No
2	0.05	0.10	No
3	0.10	0.20	No
4	0.02	0.04	Yes

$$\begin{aligned}
B_x &= 0, \\
B_y &= \begin{cases} \sin\left(\dfrac{\pi x}{2\lambda}\right), & |x| \leqslant \lambda, \\ 1, & x > \lambda, \\ -1, & x < -\lambda, \end{cases} \\
B_z &= \sqrt{1 - B_x^2 - B_y^2},
\end{aligned} \tag{2}$$

where λ denotes the half-width of the CS, which is set as 0.1. To approximate the chromosphere, transition region, and corona, the initial density distribution follows Takasao et al. (2015), namely,

$$\rho(y) = \rho_{chr} + \frac{\rho_{cor} - \rho_{chr}}{2}\left[\tanh\left(\frac{y - h_{chr}}{l_{tr}} + 1\right)\right], \tag{3}$$

where $\rho_{cor} = 1$, $\rho_{chr} = 10^5$, $h_{chr} = 0.1$, and $l_{tr} = 0.02$. Fast reconnection is initially triggered by a localized anomalous resistivity, and thus the resistivity distribution is

$$\eta = \begin{cases} \eta_b + \eta_a \exp\left[-\dfrac{x^2 + (y - h_\eta)^2}{l_\eta^2}\right], & t \leqslant t_\eta, \\ \eta_b, & t > t_\eta, \end{cases} \tag{4}$$

where $\eta_a = 5 \times 10^{-4}$, $h_\eta = 0.5$, $l_\eta = 0.03$, $t_\eta = 5$, and the background resistivity is uniformly set as $\eta_b = 5 \times 10^{-6}$ to simulate a high-Lundquist-number environment. Physically, the localized anomalous resistivity can be caused by microscopic instabilities in the CS such as lower-hybrid drift and/or ion acoustic instabilities, which can boost the process of reconnection (Yokoyama & Shibata 2001). Because $\eta_a \gg \eta_b$, the anomalous resistivity dominates the evolution during $t < t_\eta$, which provides similar initial states at $t = t_\eta$ for the cases listed in Table 1. The background pressure p_b is uniform to obtain a static initial state and is assigned as shown in Table 1. The boundary conditions are arranged as follows. The left ($x = -1$) and right ($x = 1$) are free boundaries, the top ($y = 4$) is the no-inflow boundary, and the bottom ($y = 0$) is the symmetric boundary. To reduce the influences of numerical boundaries, we only use data in the region defined by $x \in [-0.5, 0.5]$ and $y \in [0, 2]$ for analysis.

The above system is numerically solved with Athena 4.2 (Stone et al. 2008). We use the HLLD Riemann solver (Miyoshi & Kusano 2005), three-order piecewise parabolic flux reconstruction algorithm (Stone et al. 2008), and the Corner Transport Upwind method (Gardiner & Stone 2008) to solve the conservation part of Equation (1). The resistivity and TC

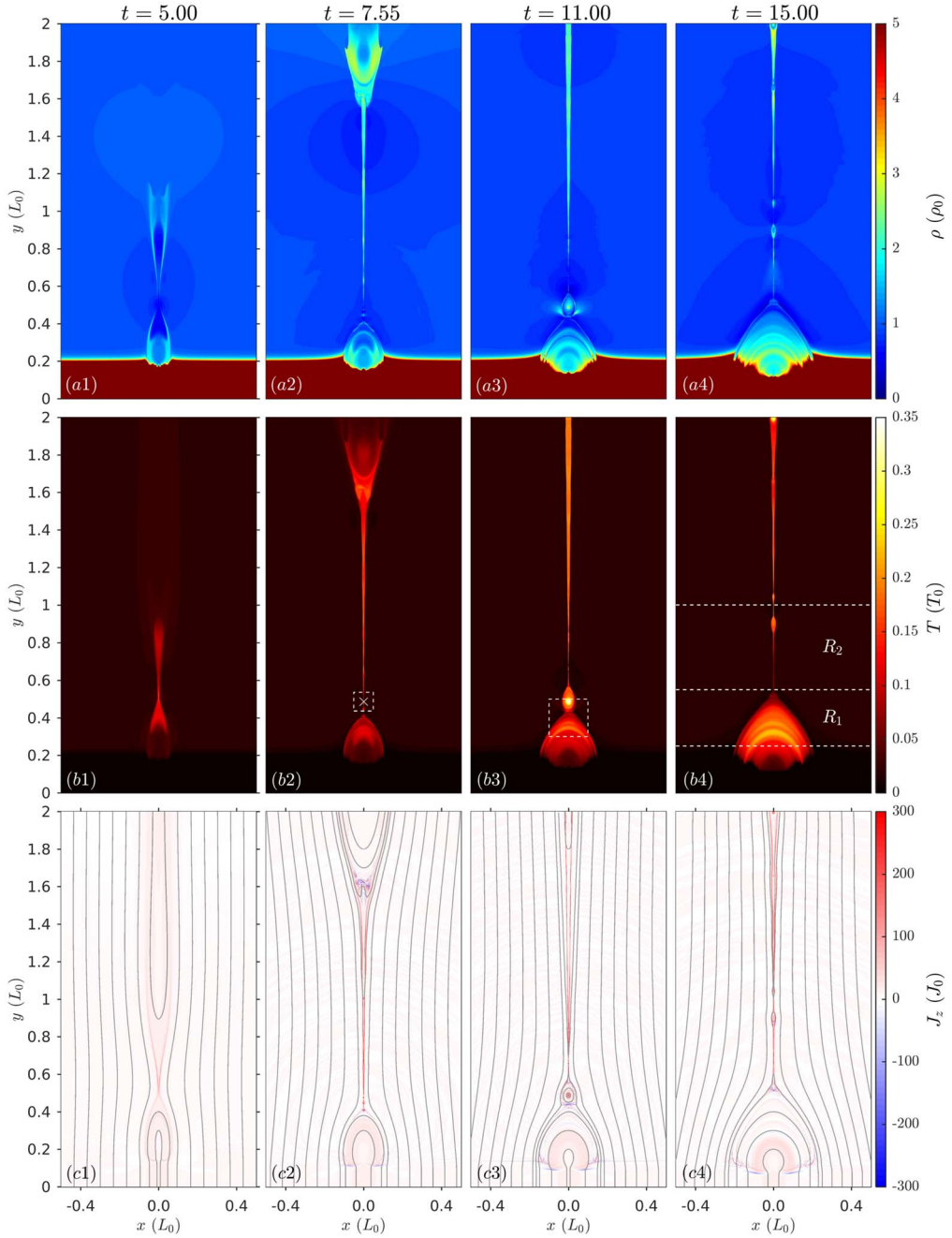

Figure 1. Snapshots of mass density ρ, temperature T, and current density J_z at four typical moments for Case 4. The first column at $t = 5$ shows the initial status when the localized anomalous resistivity is shut down. The erupting plasmoid, the stretched main CS, and the flare loop "seed" are clearly displayed by the second column at $t = 7.55$. The third column records the moment when a relatively large magnetic island starts to collide with the loop-top flux at $t = 11$. The fourth column exhibits the final state of the flare-loop systems at $t = 15$. The X-marker and the dashed box in (b2) denote, respectively, the principal X-point in the main CS and the inflow region for calculating the averaged magnetic strength and Alfvén speed in Equation (5). The dashed box in (b3) marks the loop-top region analyzed in Figure 3. The three dashed horizontal lines in (b4), namely $y = 0.25$, $y = y_{\rm lt}(t)$, and $y = 1$, define the loop-top region, R_1, and the principal reconnection site in the main CS, R_2. Here, $y_{\rm lt}(t)$ denotes the height of the top of the cusp-shaped loops, which dynamically changes with the evolution of the system. An animation of the mass density ρ, temperature T, and current density J_z for Case 4 is available online. The animation proceeds from $t = 0$ to 15.

(An animation of this figure is available.)

are calculated by the explicit operator splitting method. To suppress numerical dissipation and get a uniformly high resolution (Shen et al. 2011; Ye et al. 2020), we set high-precision uniform Cartesian grids, namely 3840 and 7680 grids on the x and y directions, respectively. The corresponding pixel scales in two directions are $\Delta x = \Delta y = 26$ km. The maximum simulation time in our simulation is $t_{\rm max} = 15$, which corresponds to 28.65 minutes in physical time.

3. Results

3.1. Overview

Figure 1 shows four typical snapshots of density ρ, temperature T, and out-of-plane current J_z for Case 4. Before $t = 5$, the reconnection is dominated by the anomalous resistivity at $y = 0.5$, where the main CS is squeezed. After $t = 5$, the anomalous resistivity is set to zero and the

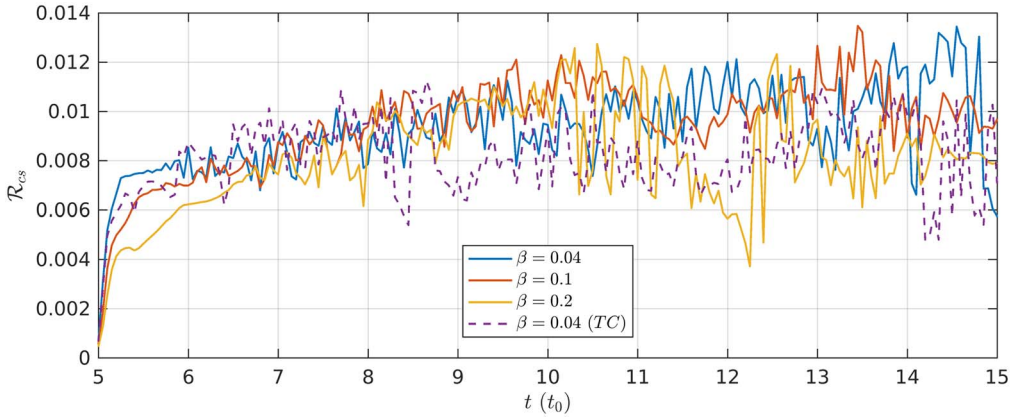

Figure 2. Evolutions of the magnetic reconnection rate in the main CS. The blue, orange, and yellow solid curves show $\mathcal{R}_{cs}(t)$ for Cases 1, 2, and 3, respectively, while the purple dashed curve presents Case 4 in which TC is considered. Here we only exhibit the reconnection rate after $t = 5$, because it is dominated by the anomalous resistivity before $t = 5$.

reconnection is determined by the uniform background resistivity η_b. At $t = 5$, a plasmoid grows above the X-point and starts to move upward, while the lower part of the main CS forms a "seed" of flare loops with two foot-points line-tied in the high-density chromosphere (first column of Figure 1). At the eruption of the upper plasmoid, the main CS is rapidly stretched (second column of Figure 1). When its aspect ratio is large enough, the main CS is quickly split by the plasmoid instability (also see Shen et al. 2011). Downflow magnetic islands carrying substantial kinetic and thermal energies are intermittently formed and then collide with the cusp-shaped flare loops. At $t = 11$, a relatively large magnetic island starts to interact with the loop-top flux (third column of Figure 1) and disappears at $t = 11.65$. Fed by the downflow islands, the flare loops also manifest an obvious expansion. At $t = 15$, the simulation stops and the flare loops evolve into their final states (fourth column of Figure 1). The distributions of density and temperature are consistent with the results of Ye et al. (2020) and highly resemble observed flare loops (e.g., Sun et al. 2014).

3.2. Reconnection in the Main CS

We first estimate the reconnection rate in the main CS as shown by the area R_2 in Figure 1(b4). It is represented by the reconnection electric field at the principal X-point (see also Yokoyama & Shibata 2001), namely,

$$\mathcal{R}(t) = \frac{\max\left(\eta_b |J_{\rm zxp}(t)|\right)}{B_{\rm in}(t)\, u_{\rm in}(t)}, \tag{5}$$

where $J_{\rm zxp}$ denotes the out-of-plane current density at the X-points, $\max(\cdot)$ means taking the maximum value in the target CS region, and $\mathcal{R}$ is normalized by the product of inflow magnetic strength $B_{\rm in}$ and Alfvén speed $u_{\rm in}$, which are averaged in the adjacent region of the principal X-point defined by $x \in [-0.05, 0.05]$ and $y \in [y_{\rm xp} - 0.05, y_{\rm xp} + 0.05]$ (see Figure 1(b2)). Here, $y_{\rm xp}$ denotes the y-coordinate of the principal X-point. The null points are determined by the method developed by Parnell et al. (1996).

For each simulation case, the reconnection rate in the main CS, $\mathcal{R}_{\rm cs}$, shows a similar trend of evolution (Figure 2). To be specific, the average value of $\mathcal{R}_{\rm cs}$ first rises quickly and then reaches its peak value, which is on the order of 0.01. We can see significant oscillations in the $\mathcal{R}_{\rm cs}$ curves, which correspond to the formation of magnetic islands (Yokoyama & Shibata 2001). The overall evolution of the reconnection rate in the main CS is consistent with previous numerical results of 2D reconnection (e.g., Ni et al. 2012; Huang & Bhattacharjee 2016; Zenitani & Miyoshi 2020). Changes to β mainly affect the initial rising stage before $t = 7$. With the increase of β, the reconnection rate at this stage becomes smaller. However, when the reconnection is fully developed ($t > 10$), the evolution of $\mathcal{R}_{\rm cs}$ is less affected by β. After including TC, the reconnection rate before $t = 6$ gets smaller and the average value also decreases slightly after $t = 10$ (Figure 2).

3.3. Second Reconnection of Magnetic Islands

To study the loop-top annihilation of magnetic islands in detail, we analyze a typical event that appears at $t \in [11, 11.65]$ in Case 4 (third column of Figure 1). As the magnetic island collides with the loop-top flux, a horizontal CS forms (see Figure 1(c3) and Figure 3(a)). Correspondingly, a pair of horizontal jets appear and quickly move along two opposite directions (Figure 3(b)). The peak speed of these jets reaches 0.8, which is of a similar order as the fastest downflow in the main CS. When these horizontal jets encounter the edge of the flare loop, they start to move downward, leading to an increase of downward speed u_y (Figure 3(c)), as observed by Tian et al. (2014). It is thus clearly revealed that the second reconnection enables the magnetic island annihilation at the flare loop top. During the second reconnection of islands, new small-scale magnetic islands are also generated in the loop-top CSs (see Figures 3(a) and (b)), similar to the "fragmenting coalescence" picture proposed by Bárta et al. (2011).

To estimate the reconnection rate of the horizontal CS, we trace it using a box with a height of 0.008 and width of 0.05 (see Figure 3(a)). After locating all X-points in this region, we use Equation (5) to estimate $\mathcal{R}_{\rm lt}$, the reconnection rate in the horizontal CS. It is shown that, as the magnetic island annihilates, the height of the horizontal CS keeps decreasing (Figure 3(d)). While for the reconnection rate within, it first increases, then reaches its peak value, and finally decreases (Figure 3(d)). Obviously, the peak reconnection rate is comparable with that in the main vertical CS. We also analyze a similar event in Case 1 where TC is not considered (see Figures 3(e)–(h)). It is found that the evolution of the horizontal CS, outjets, and the reconnection rate are similar to Case 4.

We further study the energy conversion during the second reconnection at the loop-top region and compare it with that in

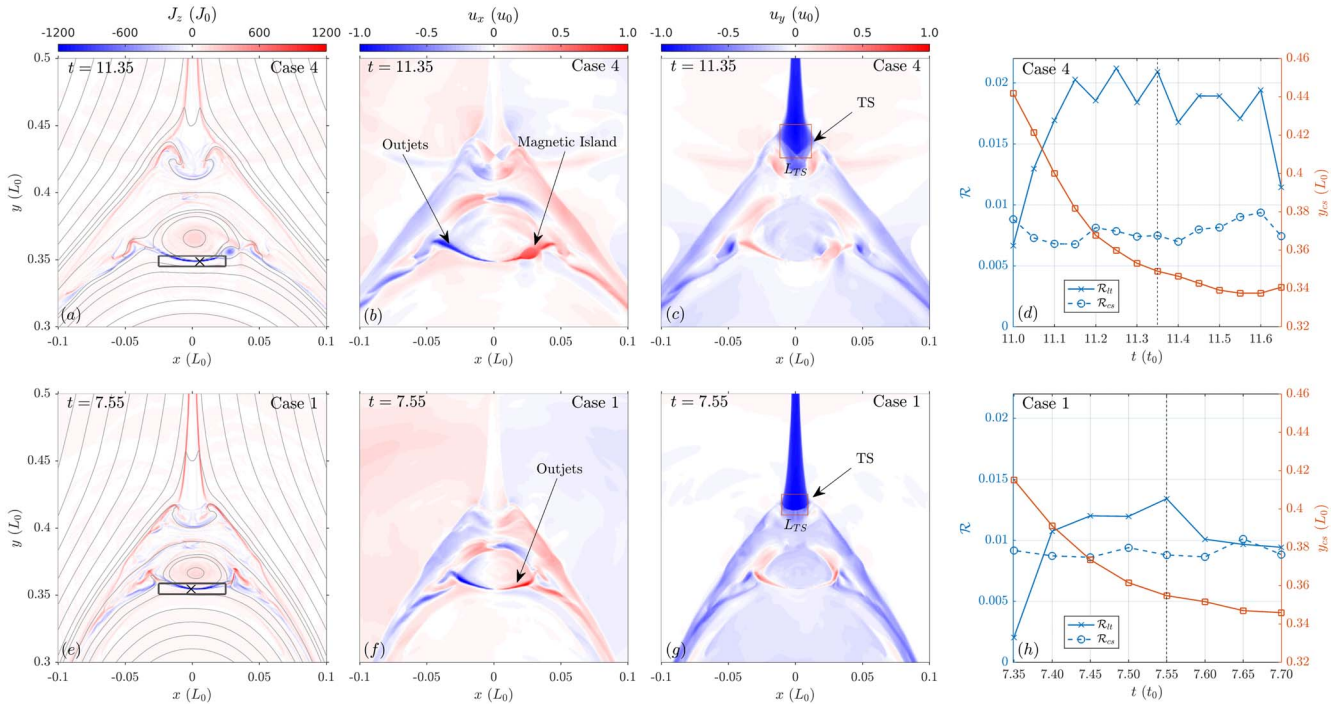

Figure 3. Two typical magnetic island annihilation events in Case 4 and Case 1. Panels (a), (b), and (c) draw the current, the horizontal velocity, and the vertical velocity around the peak time of $\mathcal{R}_{\rm lt}$. In panel (d), the blue and orange solid curves plot the reconnection rate $\mathcal{R}_{\rm lt}$ and the height of CSs, respectively, and the dashed blue curve depicts the reconnection rate $\mathcal{R}_{\rm cs}$ in the main CS. The box and "X" symbol in panel (a) mark the horizontal CS and the principal X-point, respectively. The principal TS is marked by the box in panel (c) and the spatial scale of the TS is approximately represented by its scale along the x-direction. Panels (e)–(f) display a similar event in Case 1 where TC is not included.

the main CS. In an area S, the effective changing rates of the magnetic, kinetic, and internal energies are, respectively, defined by (Forbes 1988)

$$\tilde{P}_m = \frac{\mathrm{d}}{\mathrm{d}t}\int_S \frac{B^2}{2}\mathrm{d}x\mathrm{d}y + \oint_{\partial S}(\boldsymbol{E}\times\boldsymbol{B})\cdot\boldsymbol{n}\mathrm{d}l, \quad (6)$$

$$\tilde{P}_k = \frac{\mathrm{d}}{\mathrm{d}t}\int_S \frac{\rho u^2}{2}\mathrm{d}x\mathrm{d}y + \oint_{\partial S}\frac{\rho u^2}{2}\boldsymbol{u}\cdot\boldsymbol{n}\mathrm{d}l, \quad (7)$$

$$\tilde{P}_i = \frac{\mathrm{d}}{\mathrm{d}t}\int_S \frac{p}{\gamma-1}\mathrm{d}x\mathrm{d}y + \oint_{\partial S}\frac{\gamma p}{\gamma-1}\boldsymbol{u}\cdot\boldsymbol{n}\mathrm{d}l, \quad (8)$$

where ∂S denotes the boundary, $\boldsymbol{E}=\eta\boldsymbol{J}-\boldsymbol{u}\times\boldsymbol{B}$ is the electric field, $\boldsymbol{n}$ is the unit normal vector on the boundary, and dl denotes the line element. The negative value of $\tilde{P}_m$ implies the release of magnetic energy. We calculate the evolutions of $\tilde{P}_m$, $\tilde{P}_k$, and $\tilde{P}_i$ at the loop-top region, R_1, and that in the main CS, R_2 (see Figure 1(b4)). It is found that, during most of the time, the magnetic energy release is dominated by the main CS reconnection, especially during the early stage (Figure 4(a)). However, the second reconnection at the loop-top region is able to further release magnetic energy (see negative spikes of solid curves in Figure 4(a)). For example, in Case 4, during $t\in[11, 11.65]$, the effective magnetic energy release rate in R_1 reaches about half of that in the main CS (Figure 4(a)). In R_2, the evolutions and magnitudes of $\tilde{P}_k$ and $\tilde{P}_i$ are similar (see dashed curves in Figures 4(b) and (c)), which shows that magnetic energy keeps converting to kinetic and internal energies. However, in R_1 the energy conversion process is relatively complicated. When a magnetic island enters R_1, its velocity is damped by the magnetic tension force of the flare loop. As a result, during the second reconnection, $\tilde{P}_k$ is mostly negative (see solid curves in Figure 4(b)); the magnetic energy and kinetic energy significantly increase the internal energy (see positive peaks of $\tilde{P}_i$ in Figure 4(c)). Furthermore, the time-integrated effective changes of magnetic, kinetic, and internal energies during $t\in[5, 15]$ are calculated by $\tilde{W}_m=\int_5^{15}\tilde{P}_m\mathrm{d}t$, $\tilde{W}_k=\int_5^{15}\tilde{P}_k\mathrm{d}t$, and $\tilde{W}_i=\int_5^{15}\tilde{P}_i\mathrm{d}t$, respectively. For Case 4, the $\tilde{W}_m$ released in R_1 is 13.7% of that in R_2 (see Table 2), which shows that the total release of magnetic energy during solar flares is dominated by the reconnection in the main CS region and further replenished by that at the loop-top region. In R_2, about half of the released magnetic energy is converted to internal energy and half becomes kinetic energy. However, in R_1 the main increment of the internal energy (about 72.5%) is due to magnetic energy release and the rest is from the damping of kinetic energy.

The magnetic energy cascading at the loop-top region is closely related to the distribution of the corresponding magnetic islands. The loop-top magnetic islands generated during the second reconnection can be characterized by the evolution of the cumulative distribution function (CDF) of island flux $N(\psi, t)$, which measures the number of islands with flux $\geqslant\psi$ at moment t (Figure 4(d)). When the downflow

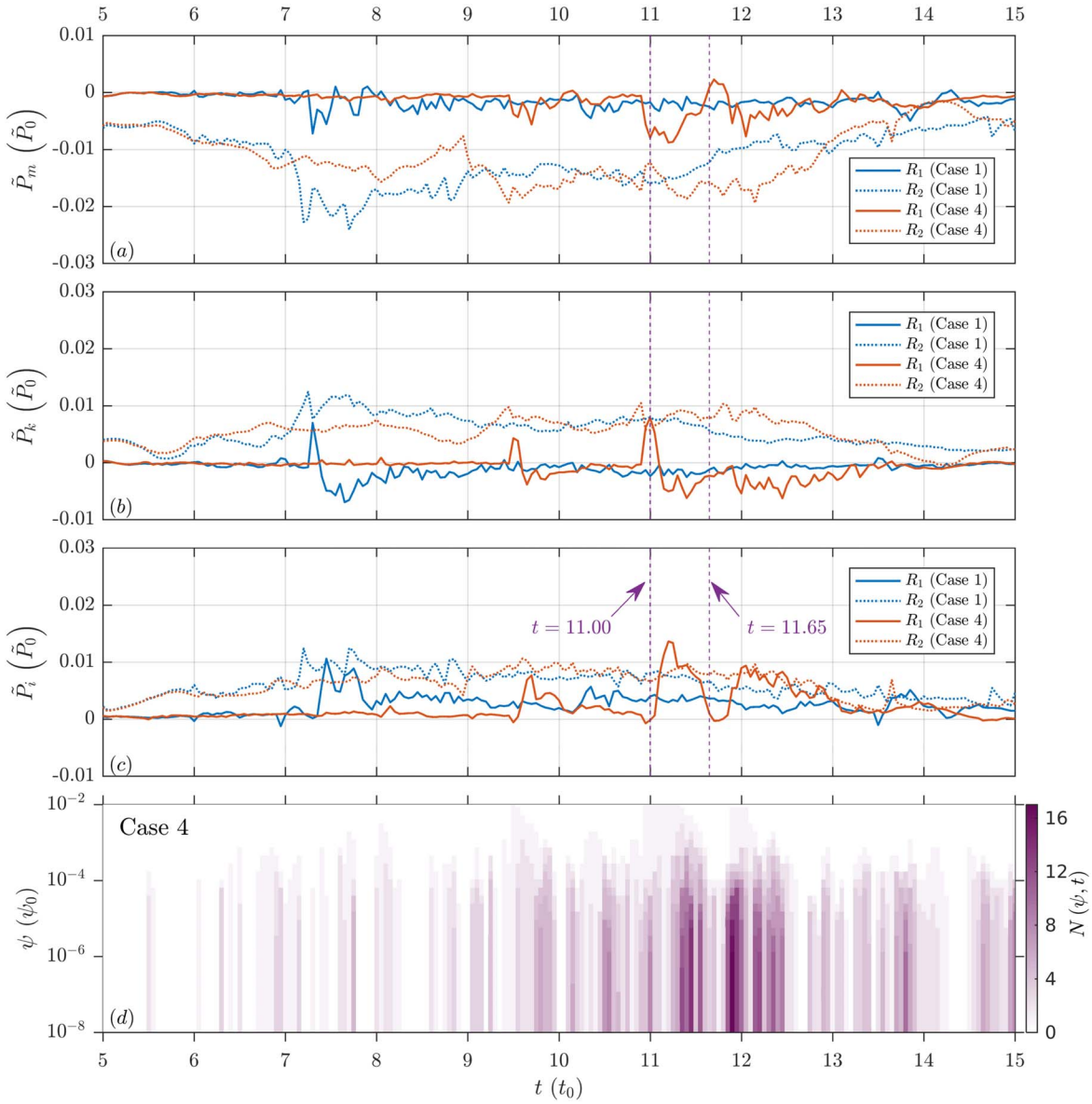

Figure 4. Illustrations of the energy conversion and magnetic island distribution of the second reconnection at the flare loop top. Panels (a), (b), and (c) show, respectively, the evolutions of the effective changing rate of magnetic, kinetic, and internal energy in the main CS and at the flare loop top. The orange (blue) curves show the results with (without) TC. For each case, the solid and dashed curves depict the evolution of $\tilde{P}$ in regions R_1 and R_2, respectively. The physical unit of $\tilde{P}$ is 6.94×10^{18} erg/(cm · s). Panel (d) depicts the CDF of magnetic island flux $N(\psi, t)$ at loop-top region R_1 in Case 4. To obtain $N(\psi, t)$, we set 30 bins spaced uniformly in $\log(\psi)$ over a range $\psi \in [10^{-8}, 0.0215]$ in units of $\psi_0 = 10^{11}$ Mx cm^{-1}.

Table 2
Time-integrated Increments of Magnetic, Kinetic, and Internal Energies in Regions R_1 and R_2 for Case 4

Region	R_1	R_2
$\tilde{W}_m$	−0.0153	−0.1115
$\tilde{W}_k$	−0.0091	0.0527
$\tilde{W}_i$	0.0211	0.0582

Note. The normalizing unit of $\tilde{W}_m$, $\tilde{W}_k$, and $\tilde{W}_i$ is $W_0 = 7.96 \times 10^{20}$ erg cm^{-1}. Summations of $\tilde{W}_m$, $\tilde{W}_k$, and $\tilde{W}_i$ in both areas should be zero theoretically but small deviations may be caused by numerical errors.

magnetic islands initiate the second reconnection, as marked by negative peaks of $\tilde{P}_{R1}$, the CDF of the island flux is significantly enhanced (see duration $t \in [11, 11.65]$ in Figure 4(d) as an example). In Figure 5, we analyze the probability distribution functions (PDFs) of magnetic island area and flux at the loop-top region R_1 based on the same method widely used for calculating plasmoid PDFs in CS (e.g., Shen et al. 2013; Lynch et al. 2016; Ye et al. 2019). The PDF of the magnetic island flux, $f(\psi)$, is determined by $f(\psi) = \mathrm{d}N_\tau(\psi)/\mathrm{d}\psi$, where $N_\tau(\psi) = \int N(\psi, t)\mathrm{d}t$ and the integration is taken over duration $t \in [5, 15]$. We also normalize the PDF to satisfy $\int f(\psi)\mathrm{d}\psi = 1$. The procedure is similar for calculating $f(S)$, the PDF of the island area. For most of the sample domain, namely $S < 10^3$ and $\psi < 10^{-3}$, both $f(S)$ and $f(\psi)$ follow a power law independent to β and TC. The slopes of the PDFs vary from -1 to -2 as the island scale increases. For the large-scale end, the PDFs slightly vary for different cases, but may be unreliable because the number of large-scale islands we collected is very limited.

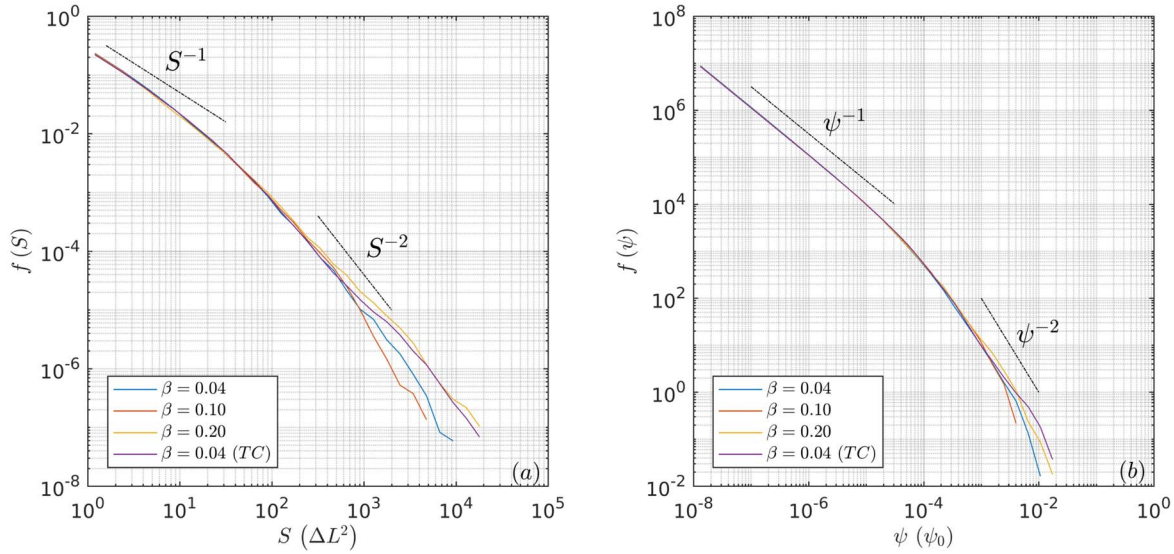

Figure 5. PDFs of magnetic island area (a) and flux (b) in the loop-top region R_1. To obtain the CDF of the area, we set 30 bins spaced uniformly in $\log(S)$ over a range $S \in [1, 2.1 \times 10^4]$ in units of $\Delta L = \Delta x \Delta y$. The configuration for calculating the CDF of the flux is the same as Figure 4(b).

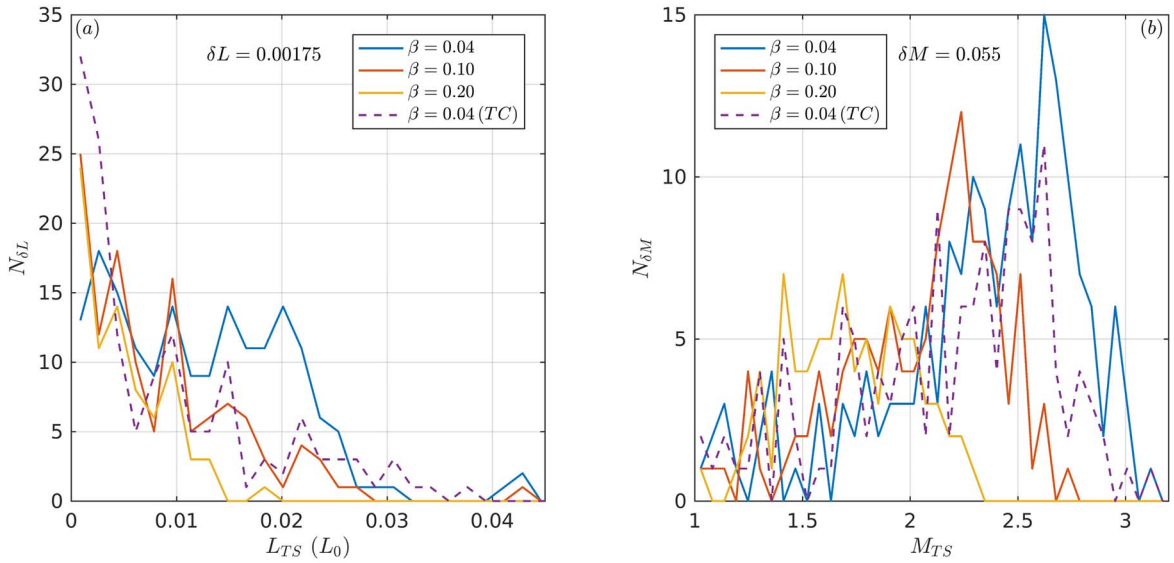

Figure 6. Histograms of spatial scale and maximum Mach number of TSs at the loop top for all simulation cases. As shown in Figures 3(c) and (g), at each moment we recognize the TS at the loop top by a box. We then measure the scale along the x-direction, $L_{\rm TS}$, as an approximation of the spatial scale of the TS. The strength of the TS is approximated by the maximum fast mode Mach number, $M_{\rm TS}$, near the front of the TS. Furthermore, we uniformly sample 200 snapshots in the time period of $t \in [5, 15]$ and count the TS in each snapshot. The bin width for panel (a) is $\delta L = 0.00175$ and for that in panel (b) is $\delta M = 0.055$.

3.4. Formation of Termination Shocks

As predicted by the standard model, the reconnection downflows may drive a TS (Forbes & Priest 1983; Forbes 1986; Forbes & Malherbe 1986, 1991; Yokoyama & Shibata 1997, 1998, 2001; Shen et al. 2018; Kong et al. 2019, 2020). Here, we further study the influences of β and TC on the formation of TSs. Because the TS is highly dynamic, in particular, it could be fragmented as the magnetic islands pass (see Shen et al. 2018); we mainly focus on the principal TS, namely the largest and strongest segment of the TS front (see Figures 3(c) and (g)). Without TC, the scale and strength of the principal TSs both decrease with the increase of β (Figure 6). Further, after TC is considered, although the histogram of $M_{\rm TS}$ is similar to that without TC (see the blue and purple curves in Figure 6(b)), the distribution of $L_{\rm TS}$ concentrates toward the lower end. This shows that an increase of β and TC can suppress the scale and strength of TSs.

4. Summary and Discussion

In this paper, we study the loop-top annihilation of magnetic islands formed in the main vertical CS in detail. Besides the reconnection in the main eruption CS, we find that reconnection also occurs at the flare loop top, as illuminated by Bárta et al. (2011). The corresponding reconnection rate is found to be of the same magnitude as that in the main CS. Interestingly, this process is highly similar to the magnetic reconnection taking place in the Earth's magnetotail (Wang et al. 2010, 2016; Lu et al. 2015). We thus suggest that magnetic island annihilation at the flare loop top, as revealed here but neglected in the standard flare model, plays a nonnegligible

role in further releasing magnetic energy so as to heat flare plasma and accelerate particles.

The fast magnetic reconnection in the main CS is dominated by the generation of plasmoids, which subsequently move quickly upward and downward along the CS. This is largely in agreement with previous results (e.g., Bhattacharjee et al. 2009; Shen et al. 2011, 2018; Kong et al. 2019, 2020) and implies the existence of fine structures in the CS during solar eruptions. The second reconnection, characterized by horizontal CSs, is initiated when magnetic islands collide with the flux above the flare loops. As the magnetic islands move toward the flare loop, the reconnection rate first grows and then decreases, with the peak being comparable with that in the main CS. The second reconnection also generates smaller-scale secondary magnetic islands, which enhance the turbulence and thus further facilitate the release of magnetic energy at the flare loop top. Moreover, the whole reconnection process seems to be intermittent because of the presence of magnetic islands; it is thus expected that the acceleration of nonthermal particles is intermittent. This might be used to explain the QPPs observed during flares.

The cascading law of magnetic islands at the loop top seems to be less affected by background β or TC. The PDF of the magnetic island flux generated during the second reconnection follows a power law varying from $f(\psi) \sim \psi^{-1}$ to ψ^{-2}, similar to the PDF of the magnetic island flux in the main CS obtained by Loureiro et al. (2012), Shen et al. (2013), and Lynch et al. (2016). However, for the spatial scale and strength of the TSs formed by the downward outflows or plasmoids, it is found that both decrease with an increase of plasma β or when including TC.

It is worth mentioning that simulations of magnetic reconnection depend on the spatial resolution. The results presented here are obtained under a high-resolution spatial grid (3840×7680), which can realize simulations with background $S = 10^6$, as discussed by Ye et al. (2020). The thickness scales of CSs in both R_1 and R_2 are on the order of 0.01, which is 0.5% of the x-domain (see Figure 1 and Figure 3). Under the current resolution, the CS thickness can be resolved by about 20 grids. Furthermore, the scale of the internal singular layer in classic tearing mode theory is $\delta \sim aS_a^{-1/4}$ (Pucci et al. 2017), where a denotes the width of a CS, $S_a = av_A/\eta$ is the local Lundquist, and v_A is the Alfvén speed. The number of grids resolving the inner singular layer can be estimated by

$$\frac{\delta}{\Delta L} \sim \frac{aS_a^{-1/4}}{\Delta L} = \frac{\eta^{1/4}}{\Delta L}\frac{a^{3/4}}{v_A^{1/4}}, \tag{9}$$

where ΔL denotes the dimensionless size of the mesh grid. Setting $\Delta L = 2/3840$, $\eta = 5 \times 10^{-6}$, $v_A = 1$, and $a = 0.01$, we have $\delta/\Delta L \sim 3$. It is shown that the small-scale inner singular layer can still be roughly resolved. We have also studied the influence of resolutions on our conclusions by running cases with different grid configurations. It is shown that the conclusions are only valid for relatively high-resolution simulations.

In our numerical model, the fine dynamics of the chromosphere might be inaccurate, because the effects of partially ionized plasma (PIP) are not included. It is true that partial ionization has influences on the properties of shocks, the CS structure, and fractal reconnection (Imada et al. 2011; Hillier et al. 2016). However, in this paper we mainly focus on the reconnection dynamics in the high-temperature corona. Thus, the effects of the partially ionized chromosphere on our results are very limited; the only influence is on the structure and dynamics of the post-flare loops into which the chromospheric plasma is evaporated.

We would like to thank the anonymous referee for valuable suggestions. This research is supported by Natural Science Foundation of China grant Nos. 11722325, 11733003, 11790303, 11790300, and 11805203.

ORCID iDs

Yulei Wang https://orcid.org/0000-0001-9863-5917
Xin Cheng https://orcid.org/0000-0003-2837-7136
Mingde Ding https://orcid.org/0000-0002-4978-4972
Quanming Lu https://orcid.org/0000-0003-3041-2682

References

Aurass, H., & Mann, G. 2004, ApJ, 615, 526
Bárta, M., Büchner, J., Karlický, M., & Skála, J. 2011, ApJ, 737, 24
Bhattacharjee, A., Huang, Y.-M., Yang, H., & Rogers, B. 2009, PhPl, 16, 112102
Cai, Q., Feng, H., Ye, J., & Shen, C. 2021, ApJ, 912, 79
Cai, Q., Shen, C., Raymond, J. C., et al. 2019, MNRAS, 489, 3183
Chen, B., Bastian, T. S., Shen, C., et al. 2015, Sci, 350, 1238
Chen, P. F., Fang, C., Tang, Y. H., & Ding, M. D. 1999, ApJ, 513, 516
Cheng, X., Li, Y., Wan, L. F., et al. 2018, ApJ, 866, 64
Forbes, T. G. 1986, ApJ, 305, 553
Forbes, T. G. 1988, SoPh, 117, 97
Forbes, T. G., & Malherbe, J. M. 1986, ApJL, 302, L67
Forbes, T. G., & Malherbe, J. M. 1991, SoPh, 135, 361
Forbes, T. G., & Priest, E. R. 1983, SoPh, 84, 169
Gardiner, T. A., & Stone, J. M. 2008, JCoPh, 227, 4123
Guo, L. J., Huang, Y. M., Bhattacharjee, A., & Innes, D. E. 2014, ApJL, 796, L29
Hillier, A., Takasao, S., & Nakamura, N. 2016, A&A, 591, A112
Huang, Y.-M., & Bhattacharjee, A. 2010, PhPl, 17, 062104
Huang, Y.-M., & Bhattacharjee, A. 2012, PhRvL, 109, 265002
Huang, Y.-M., & Bhattacharjee, A. 2013, PhPl, 20, 055702
Huang, Y.-M., & Bhattacharjee, A. 2016, ApJ, 818, 20
Huang, Y.-M., Bhattacharjee, A., & Sullivan, B. P. 2011, PhPl, 18, 072109
Huang, Y.-M., Comisso, L., & Bhattacharjee, A. 2017, ApJ, 849, 75
Imada, S., Murakami, I., Watanabe, T., Hara, H., & Shimizu, T. 2011, ApJ, 742, 70
Kong, X., Guo, F., Shen, C., et al. 2019, ApJL, 887, L37
Kong, X., Guo, F., Shen, C., et al. 2020, ApJL, 905, L16
Kopp, R. A., & Pneuman, G. W. 1976, SoPh, 50, 85
Lin, J., & Forbes, T. G. 2000, JGR, 105, 2375
Lin, J., Murphy, N. A., Shen, C., et al. 2015, SSRv, 194, 237
Loureiro, N. F., Samtaney, R., Schekochihin, A. A., & Uzdensky, D. A. 2012, PhPl, 19, 042303
Loureiro, N. F., & Uzdensky, D. A. 2015, PPCF, 58, 014021
Lu, S., Lu, Q., Lin, Y., et al. 2015, JGRA, 120, 6286
Lynch, B. J., Edmondson, J. K., Kazachenko, M. D., & Guidoni, S. E. 2016, ApJ, 826, 43
Miyoshi, T., & Kusano, K. 2005, JCoPh, 208, 315
Ni, L., Ziegler, U., Huang, Y.-M., Lin, J., & Mei, Z. 2012, PhPl, 19, 072902
Parnell, C. E., Smith, J. M., Neukirch, T., & Priest, E. R. 1996, PhPl, 3, 759
Priest, E., & Forbes, T. 2000, Magnetic Reconnection: MHD Theory and Applications (Cambridge: Cambridge Univ. Press)
Pucci, F., & Velli, M. 2013, ApJL, 780, L19
Pucci, F., Velli, M., & Tenerani, A. 2017, ApJ, 845, 25
Ruan, W., Xia, C., & Keppens, R. 2020, ApJ, 896, 97
Samtaney, R., Loureiro, N. F., Uzdensky, D. A., Schekochihin, A. A., & Cowley, S. C. 2009, PhRvL, 103, 105004
Shen, C., Kong, X., Guo, F., Raymond, J. C., & Chen, B. 2018, ApJ, 869, 116
Shen, C., Lin, J., & Murphy, N. A. 2011, ApJ, 737, 14
Shen, C., Lin, J., Murphy, N. A., & Raymond, J. C. 2013, PhPl, 20, 072114
Stone, J. M., Gardiner, T. A., Teuben, P., Hawley, J. F., & Simon, J. B. 2008, ApJS, 178, 137

Sun, J. Q., Cheng, X., & Ding, M. D. 2014, ApJ, 786, 73
Takasao, S., Matsumoto, T., Nakamura, N., & Shibata, K. 2015, ApJ, 805, 135
Takasao, S., & Shibata, K. 2016, ApJ, 823, 150
Tian, H., Li, G., Reeves, K. K., et al. 2014, ApJL, 797, L14
Tsuneta, S., & Naito, T. 1998, ApJL, 495, L67
Uzdensky, D. A., Loureiro, N. F., & Schekochihin, A. A. 2010, PhRvL, 105, 235002
Wang, R., Lu, Q., Du, A., & Wang, S. 2010, PhRvL, 104, 175003
Wang, R., Lu, Q., Nakamura, R., et al. 2016, NatPh, 12, 263
Ye, J., Cai, Q., Shen, C., et al. 2020, ApJ, 897, 64
Ye, J., Shen, C., Raymond, J. C., Lin, J., & Ziegler, U. 2019, MNRAS, 482, 588
Yokoyama, T., & Shibata, K. 1997, ApJL, 474, L61
Yokoyama, T., & Shibata, K. 1998, ApJL, 494, L113
Yokoyama, T., & Shibata, K. 2001, ApJ, 549, 1160
Zenitani, S., & Miyoshi, T. 2020, ApJL, 894, L7
Zhao, X., & Keppens, R. 2020, ApJ, 898, 90